

Article

Numerical Alloy Development for Additive Manufacturing towards Reduced Cracking Susceptibility

Benjamin Wahlmann ^{*}, Dominik Leidel, Matthias Markl  and Carolin Körner

Department of Materials Science, Friedrich-Alexander-Universität Erlangen-Nürnberg, Martensstr. 5, D-91058 Erlangen, Germany; dominik.leidel@fau.de (D.L.); matthias.markl@fau.de (M.M.); carolin.koerner@fau.de (C.K.)

* Correspondence: benjamin.wahlmann@fau.de

Abstract: In this work, we investigated the viability of established hot cracking models for numerically based development of crack-resistant nickel-base superalloys with a high γ' volume fraction for additive manufacturing. Four cracking models were implemented, and one alloy designed for reduced cracking susceptibility was deduced based on each cracking criterion. The criteria were modeled using CALPHAD-based Scheil calculations. The alloys were designed using a previously developed multi-criteria optimization tool. The commercial superalloy Mar-M247 was chosen as the reference material. The alloys were fabricated by arc melting, then remelted with laser and electron beam, and the cracking was assessed. After electron beam melting, solidification cracks were more prevalent than cold cracks, and vice versa. The alloys exhibited vastly different crack densities ranging from 0 to nearly 12 mm^{-1} . DSC measurements showed good qualitative agreement with the calculated transition temperatures. It was found that the cracking mechanisms differed strongly depending on the process temperature. A correlation analysis of the measured crack densities and the modeled cracking susceptibilities showed no clear positive correlation for any crack model, indicating that none of these models alone is sufficient to describe the cracking behavior of the alloys. One experimental alloy showed an improved cracking resistance during electron beam melting, suggesting that further development of the optimization-based alloy design approach could lead to the discovery of new crack-resistant superalloys.

Keywords: nickel-base alloys; CALPHAD; alloy development; hot cracking



Citation: Wahlmann, B.; Leidel, D.; Markl, M.; Körner, C. Numerical Alloy Development for Additive Manufacturing towards Reduced Cracking Susceptibility. *Crystals* **2021**, *11*, 902. <https://doi.org/10.3390/cryst11080902>

Academic Editor: Bolv Xiao

Received: 27 June 2021
Accepted: 29 July 2021
Published: 31 July 2021

Publisher's Note: MDPI stays neutral with regard to jurisdictional claims in published maps and institutional affiliations.



Copyright: © 2021 by the authors. Licensee MDPI, Basel, Switzerland. This article is an open access article distributed under the terms and conditions of the Creative Commons Attribution (CC BY) license (<https://creativecommons.org/licenses/by/4.0/>).

1. Introduction

Nickel-base superalloys are high-performance materials that are employed in the hottest sections of jet engines and stationary gas turbines. While they are usually processed by investment casting, in recent years, additive manufacturing (AM), also known as 3D printing, of superalloys has gained increasing traction, as it allows near-net-shape fabrication of complex structures and tailoring of microstructures [1–3]. One major challenge posed by AM is the high cracking susceptibility of many commercially available alloys, such as IN738 and Mar-M247. These are often identified as solidification cracks, which develop during the cooling of the alloy due to the presence of liquid films at the grain boundaries [4–6]. Additionally, liquation cracking [7] and strain age cracking in the solid state [8] have been observed. In this study, we focus on solidification cracking, since this appears to be the most predominantly discussed mechanism in the context of AM. Although there is no consensus on the exact formation process of these cracks [9] and the types of cracks vary depending on the material and process conditions, two factors seem to play important roles: the alloy's solidification range and the presence of large amounts of γ' phase. This intermetallic phase, with the ordered $L1_2$ structure, has the stoichiometric composition $\text{Ni}_3(\text{Al}, \text{Ti})$. Due to its stability at high temperatures, this phase is responsible for the high-temperature strength of nickel-base superalloys. At room temperature, typically 60–70% of γ' phase is present.

Nickel-base alloys are typically considered unweldable if the sum of the γ' -forming elements Al and Ti exceeds 6 wt.% [10], since such alloys are sensitive to cracking. Most superalloys for turbine blade applications fall into this category. This also applies to AM techniques such as selective laser melting (SLM) and selective electron beam melting (SEBM). In these AM processes, parts are fabricated by subsequently welding layers of powder on top of each other. Due to thermal gradients in the material, the upper layers of an AM part are subject to tensile stresses [11], since the shrinkage of a layer during cooling is limited by the lower, already solidified layers.

Due to shrinkage by cooling and solidification, neighboring grains are subjected to tensile strain. Solidification cracking can occur during the final stage of solidification if the cohesion between grains is too low to withstand the strain. According to Chauvet et al. [9], high-angle grain boundaries are less stable in this regard than low-angle boundaries. This feature can be tailored by appropriate process design. During cooling, segregation of low-melting elements to the melt leads to a depression of the solidus temperature compared to equilibrium solidification. Several characteristics of the resulting solid fraction-temperature curve, such as steepness and the solidification interval over a specific solid fraction range, are considered major influences on the cracking behavior. They will be discussed in detail in Section 2.1. These characteristics are determined by the alloy composition, and thus can be engineered by alloy design.

The composition of nickel-base superalloys is fine-tuned to enable them to operate under harsh conditions of high temperature and stress. New alloys were initially developed by trial and error, relying on experience and qualitative assessments of the influence of alloying elements. Since the design space is large (typical alloys are composed of 8–10 elements) and properties are very sensitive to the variation of elements, numerous trials are necessary to arrive at a suitable composition.

Alternative systematic computational approaches were developed by the Advanced Alloy Design Program (AADP) at the National Institute for Materials Science in Japan [12] and Reed et al. [13–15]. These methods employ regression models and CALPHAD (CALculation of PHase Diagrams) calculations to predict alloy properties and calculate merit functions, which qualitatively describe phenomena such as creep resistance that would otherwise require complex simulations. The design space is sampled along a regular grid and alloy properties are calculated for each grid point. Candidate alloys for experimental investigations are then selected by applying restrictions to the relevant properties. As these restrictions are only introduced after the design space sampling, properties for many unsuitable alloy compositions are calculated.

Another design method employs genetic optimization algorithms coupled with property descriptors to search the composition space efficiently for the best desired property combinations. The alloy design task is formulated as an optimization problem by choosing suitable alloy properties as goals to be minimized or maximized. By defining constraints to the optimization problem, undesirable alloy compositions can be excluded early and the compositions are driven towards desirable compositions. This approach was first followed by Rettig [16] and Menou [17] and was developed further by Müller and Markl, who developed the optimization-based alloy design tool *MultOPT++* [18,19]. This tool has already been applied successfully for the development of a Re-free high-performance alloy [20].

While crack-resistant nickel-base alloys have been designed using CALPHAD-based property calculations, e.g., ABD-850AM and ABD-900AM [14], these alloys have a dramatically reduced γ' phase fraction and a comparatively low γ' solvus temperature of just over 1000 °C. These alloys also have lower strength at high temperature than commercial alloys such as Mar-M247, which is used in static aircraft turbine parts exposed to great mechanical loads and temperatures. There is a demand for 3D-printable alloys with a large γ' fraction and excellent high-temperature strength to reduce the costs of manufacturing such complex parts.

In this study, we investigate the viability of four hot cracking criteria published in the literature for the numerical development of crack-resistant alloys. Mar-M247 was chosen as the reference material due to its relevance in the industry and recently growing interest in additive manufacturing of this alloy and its derivatives. We chose the optimization-based design method described above due to its flexibility and higher computational efficiency compared to the sampling approach. Using a suitable formulation of the optimization problem, the γ' fraction and other key properties are kept close to those of the reference alloy. Alloys are designed based on the cracking criteria, produced, and remelted, and the cracking susceptibility is determined. We further assess the predictive capability of the cracking indicators.

2. Materials and Methods

2.1. Cracking Susceptibility Models

Four criteria for solidification cracking sensitivity of nickel-base alloys were derived from the literature. These criteria are based on the temperature T vs. solid fraction f_s curve, which can be modeled using a CALPHAD-based Scheil-Gulliver simulation [21]. All criteria must be minimized to improve cracking resistance, and they are described in detail as follows:

- Solidification interval (SI):

According to [22], the solidification interval measured by differential scanning calorimetry (DSC), shows high correlation with the observed crack density. Accordingly, the SI criterion was modeled as

$$SI = T_L - T(f_s = 0.95) \quad (1)$$

where T_L is the liquidus temperature. The solidus temperature was evaluated at $f_s = 0.95$ since the Scheil calculations were found to tend toward unrealistically low temperatures at high solid fractions. This is due to the lack of back diffusion, which leads to a worst-case estimation of the solidification interval. Furthermore, bridging between the dendrites will lead to cohesion while some liquid pockets are still present.

- Kou criterion (Kou):

Kou found that long, narrow channels between dendrites increased the likelihood of solidification cracking, since liquid feeding is impeded [23]. The shape of these channels is characterized by the steepness of the solid fraction-temperature curve:

$$Kou = \max\left(\left|\frac{dT}{df_s}\right|\right), 0.81 \leq f_s \leq 0.95. \quad (2)$$

As the intergranular channels widen due to the thermal shrinkage of the solid, sufficient liquid must flow into the channels to compensate for the shrinkage. While the model was derived from theoretical considerations, it has good predictive capability for aluminum- and nickel-base alloys [24,25].

- Critical temperature interval (CTI):

Shukla et al. [26] recently developed a semi-empirical model for cracking during AM. Part of this model is the mean slope of the curve $f_s(T)$ in a critical range of f_s , where a steep slope indicates low cracking susceptibility. Inversely, this criterion can be interpreted as the temperature interval over a given range of solid fraction:

$$CTI = T(f_s = 0.7) - T(f_s = 0.85). \quad (3)$$

In this case, a narrow temperature interval signifies good cracking resistance.

- Strain coefficient (SC):

The second part of the criterion by Shukla et al. [26] incorporates the rate of change of total strain with temperature $d\varepsilon/dT$ in the alloy near the end of solidification. The total strain

ε is composed of strain due to thermal contraction during cooling and volume shrinkage due to the liquid-solid transition [27]. The total strain is defined as

$$\varepsilon = \alpha(T(f_S = 0.8) - T(f_S = 0.95)) + \beta^{1/3}\Delta f_S \quad (4)$$

$$\beta = \frac{V_L - V_S}{V_L}$$

with the coefficient of thermal expansion α , the volume shrinkage coefficient β , and the difference of solid fractions Δf_S , at which the upper and lower temperatures are evaluated, in this case 0.15. Coefficient α is modeled with a regression model from [26], while β is calculated from the molar volumes of solid and liquid V_S and V_L computed by CALPHAD. The shrinkage coefficient criterion is then defined as

$$SC = \frac{\varepsilon}{T(f_S = 0.8) - T(f_S = 0.95)}. \quad (5)$$

The thermal expansion and volume shrinkage coefficients were calculated at the average temperature in the interval of $0.8 \leq f_S \leq 0.95$. This criterion is similar to the well-known Rappaz criterion for hot tearing, albeit in a simpler form [28].

2.2. Reference Material

The composition of the Mar-M247 reference alloy was adapted from [29]. However, minor elements that usually serve as grain boundary strengtheners (B, C, Zr) were not included. Since these elements tend to increase the solidification range, they were assumed to be detrimental to cracking susceptibility, as described by the previously defined indicators. The alloy composition is presented in Table 1. Thermodynamic calculations were also carried out excluding these elements.

Table 1. Composition of Mar-M247 reference alloy in at.%.

Element	Mar-M247
Al	12.3
Ti	1.3
Cr	9.7
Co	10.2
Mo	0.4
Ta	1.0
W	3.3
Hf	0.5
Ni	61.3

2.3. Implementation Details

The alloy design tool MultOpt++, which was previously developed in-house, was ported to *Python*. For further information on software design and verification, the reader is referred to [18,19]. CALPHAD calculations were performed with Thermo-Calc version 2020b and the TCNI9 database [30] via the Python-based *TC-Python* API. The optimization procedure was performed by the *pymoo* multi-objective optimization library for Python [31] using the NSGA-II genetic optimization algorithm [32].

2.4. Optimization

The optimization goals follow from the desired properties of the alloys: minimal cracking susceptibility and minimal deviation from crucial properties of the Mar-M247 reference alloy. The most relevant properties were determined as the liquidus temperature

T_L , the γ' solvus temperature $T_{\gamma'}$, and the γ' phase fraction at 1000 °C $\Phi_{\gamma'}$. Deviation from Mar-M247 was defined as root-mean-square deviation (RMSD):

$$RMSD = \sqrt{\frac{1}{3} \left(\left(\frac{T_L - T_L^{ref}}{T_L^{ref}} \right)^2 + \left(\frac{T_{\gamma'} - T_{\gamma'}^{ref}}{T_{\gamma'}^{ref}} \right)^2 + \left(\frac{\Phi_{\gamma'} - \Phi_{\gamma'}^{ref}}{\Phi_{\gamma'}^{ref}} \right)^2 \right)} \quad (6)$$

where the superscript *ref* indicates the respective property of the reference alloy. All property deviations were normalized with respect to the reference values calculated with Thermo-Calc to weight the property values of different magnitudes equally.

Additionally, the fraction of detrimental TCP phases (σ , μ , P, and R phase) was constrained below 1 mol-% at 800 °C. The full definition of the optimization problem is shown in Table 2. The bounds of the design variables, i.e., the element concentrations \vec{c} , cover the concentration ranges typical for nickel-base superalloys; these were adapted from [20]. The limits of element concentrations were slightly extended to allow unconventional, but possibly interesting, compositions to be selected. As in the reference alloy, minor elements were not included. Furthermore, Hf was excluded from the design variables, as it lowers the solidus temperature considerably. No further constraints describing, e.g., mechanical properties, were introduced so as to not indirectly impose bounds on the cracking indicators.

Table 2. Definition of optimization problem. *CS*, *RMSD*, *TCP*, and \vec{c} are cracking sensitivity, root-mean-square deviation from reference alloy properties, fraction of TCP phases, and entire concentration range, respectively.

Optimization Goals	Constraints
$\text{minimize} \begin{bmatrix} CS(\vec{c}) \\ RMSD(\vec{c}) \end{bmatrix}$	$TCP_{T=800\text{ }^\circ\text{C}}(\vec{c}) \leq 1 \text{ mol} - \%$
	$c(Al) \leq 15 \text{ at.} - \%$ $c(Ti) \leq 5 \text{ at.} - \%$ $c(Cr) \leq 15 \text{ at.} - \%$ $c(Co) \leq 20 \text{ at.} - \%$ $c(Mo) \leq 10 \text{ at.} - \%$ $c(Ta) \leq 10 \text{ at.} - \%$ $c(W) \leq 10 \text{ at.} - \%$

Optimization was performed for each of the four cracking sensitivity criteria with a population of 250 individuals and up to 100 iterations. Convergence was checked after the optimizations had finished using the Hypervolume indicator [33]. This indicator measures the enclosed volume between the Pareto front and a reference point. A Pareto front is considered to be better when its associated hypervolume measure is higher. All optimizations were deemed to have converged sufficiently, since the hypervolume increased only marginally at the end of the process.

2.5. Experimental Procedure

The selected alloys were arc-melted in a Bühler Arc Melter AM/05 and then machined to plates of 35 mm × 15 mm × 5 mm. For each alloy, two plates were produced.

The plates were remelted with a laser and an electron beam within an 8 × 8 mm² square. Since in powder-bed-based processes the melt pool depth is greater than the thickness of the powder layer [34], solidified material is remolten. We expected this approach to provide a suitable estimation of the cracking susceptibility in a process using powder. For each alloy, three combinations of beam power P and scan speed v were used. Laser remelting was performed in a laser metal deposition device by InssTek equipped with a 1070 nm Yb:YAG fiber laser at room temperature. Electron beam melting was performed using the ATHENE SEBM system, which is equipped with an electron gun by pro-beam

(AG & Co. KGaA, Gilching, Germany) with an acceleration voltage of 60 kV [35]. The samples were placed on a steel plate and heated uniformly using a defocused electron beam. The temperature of the build plate was measured with a thermocouple attached to the bottom of the plate. Remelting was performed after the build plate had reached a temperature of 900 °C. Due to limited heat transfer between the specimens and the build plate, the specimens had a higher temperature that could not be measured directly.

The melting conditions were determined to match the typical conditions employed in the respective processes. Three magnitudes of energy input were chosen to create different melt pool depths and thermal gradients, which were expected to affect the cracking tendency. In particular, the electron beam melting parameters were adapted from a process window for the weldable superalloy Inconel 718 [34]. The laser melting parameters were adapted from previous remelting experiments to achieve a suitable melt pool depth. The beam was directed along a snake-hatch pattern with a hatch spacing h of 350 μm for laser melting and 200 μm for electron beam melting. These parameters ensured that the melt tracks would overlap. All process parameters are listed in Table 3.

Table 3. Process parameters for laser and electron beam melting.

Beam Type	Beam Power P (W)	Scan Speed v (mm/s)	Hatch Spacing h (mm)	Energy Input (J mm^{-2}) ¹
Laser beam	300	10	0.35	85.7
	300	20	0.35	42.9
	200	10	0.35	57.7
	350	500	0.2	3.5
Electron beam	400	1000	0.2	2
	500	2000	0.2	1.25

¹ Energy input per unit area is defined as $P/(v \times h)$.

The melted samples were sectioned in the middle along the direction of the scan vectors. They were then mounted in Technovit 4071 embedding agent and ground with SiC paper up to 4000 grit, followed by subsequent polishing with 3 μm diamond suspension and colloidal silica suspension from Struers. Cracks were measured on the polished samples using a Leica DM6000M optical microscope. Cracking susceptibility was assessed by crack density, which was defined as the total crack length divided by the cross-sectional area of the melted material. The samples were etched with V2A etchant. The crack morphologies were investigated in detail with an FEI Quanta 450 scanning electron microscope (SEM) using the etched specimens. DSC measurements in the as-cast state were conducted with a Netzsch STA409 at a 5 K/min heating rate in an alumina crucible to determine the solidification intervals.

3. Results

3.1. Alloy Selection

The Pareto fronts resulting from the optimizations of cracking criteria and crucial property deviations (Equation (6)) are presented in Figure 1. The selected alloys are highlighted in red. It should be noted that the ranges of property deviations vary significantly depending on the chosen cracking criterion. All alloys were chosen so that their cracking criteria were lower than those calculated for Mar-M247.

For the SI criterion, three sections on the Pareto front can be distinguished. The SI alloy was selected as the one with the lowest mean deviation in the middle section. The SI (solidification interval) criterion value (45 °C) is considerably lower than the respective value for Mar-M247 (245 °C).

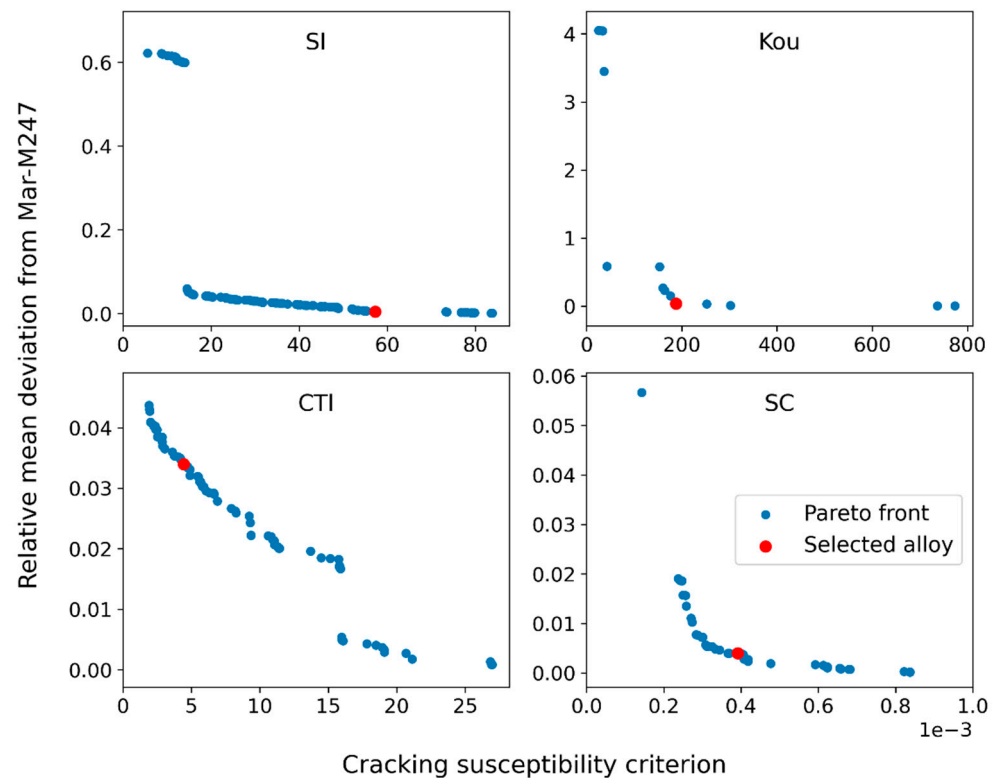


Figure 1. Pareto fronts for optimization of cracking criteria and deviation of crucial properties from Mar-M247. Cracking criteria are solidification interval (*SI*), Kou criterion (*Kou*), critical temperature interval (*CTI*), and shrinkage coefficient (*SC*), cf. Section 2.1. Cracking susceptibility values for reference alloy are: *SI*: 245 °C, *Kou*: 2305 °C, *CTI*: 400 °C, *SC*: $4.8 \times 10^{-4} \text{ K}^{-1}$.

The *Kou* criterion ($\max |dT/df_s|$) alloy was selected according to a trade-off criterion [36], which indicates Pareto-optimal solutions with good compromises between different optimization goals. The trade-off value reflects how much one goal must be worsened to achieve a particular improvement in another goal. Solutions where worsening of one goal leads to a similar increase in another goal are preferable. The selected alloy had the second-highest overall trade-off value. However, the solution with the highest value had a deviation value that was far too large at 0.58. The crack sensitivity value of the selected alloy (188 °C) was much smaller than the reference value (2305 °C).

For the *CTI* criterion, an alloy with a similar deviation value (0.06) as the *Kou* criterion was selected. Alloys in this area also showed a good tradeoff between goals. The selected alloy had a *CTI* ($T(f_s = 0.7) - T(f_s = 0.85)$) value of 4.4 °C, while the reference value is 60 °C.

Alloys with a low *SC* criterion exhibited small amounts of B2 phase precipitating from the melt. Precipitation of this phase was not considered as a constraint in the optimization. These alloys were considered unfeasible since this phase embrittles the alloy. Therefore, the alloy with the lowest *SC* value that contained no deleterious phases was selected with an *SC* value of $3.9 \times 10^{-4} \text{ K}^{-1}$, about 80% of the reference value of $4.8 \times 10^{-4} \text{ K}^{-1}$.

The compositions of the selected alloys are summarized in Table 4. It should be noted that these compositions are quite different from Mar-M247, as well as from each other. This is due to the absence of any constraints or goals relating to mechanical properties. A development program incorporating such considerations will follow.

Table 4. Composition of designed alloys in at.%.

Element	Alloy SI	Alloy Kou	Alloy CTI	Alloy SC
Al	14.0	11.7	10.9	10.4
Ti	-	1.0	-	3.9
Cr	6.5	0.3	0.4	2.1
Co	0.3	0.5	3.4	7.4
Mo	-	0.3	-	-
Ta	1.2	1.7	4.8	1.0
W	-	3.0	0.1	4.2
Hf	-	-	-	-
Ni	78.0	81.5	80.4	71.7

The equilibrium fractions of the liquid, γ , and γ' phases of all alloys were calculated with Thermo-Calc to assess the deviation of properties according to the RMSD criterion (Figure 2; dots indicate the relevant properties). The liquidus temperature of the selected alloys varied from 1402 to 1456 °C, whereas the liquidus temperature of Mar-M247 was 1390 °C. This increased temperature may be related to the overall lower concentrations of alloying elements in these alloys, as higher-alloy materials typically have lower liquidus temperatures. The γ' solvus temperature was in the range of 1250 to 1343 °C (Mar-M247: 1255 °C) and the γ' phase fractions at 1000 °C were in the range of 53.0 to 55.6% (Mar-M247: 59.3%). Mar-M247 had the highest calculated γ' fraction of all alloys, since the γ' phase is stabilized by Hf. At 10.6%, the deviation of the γ' fraction of the Kou alloy was the largest of all relative deviations. However, the absolute deviation (6.3%) was still small and probably within experimental measurement uncertainty. The equilibrium solidus temperature was consistently higher than for Mar-M247, whose solidus temperature is strongly depressed by the addition of Hf.

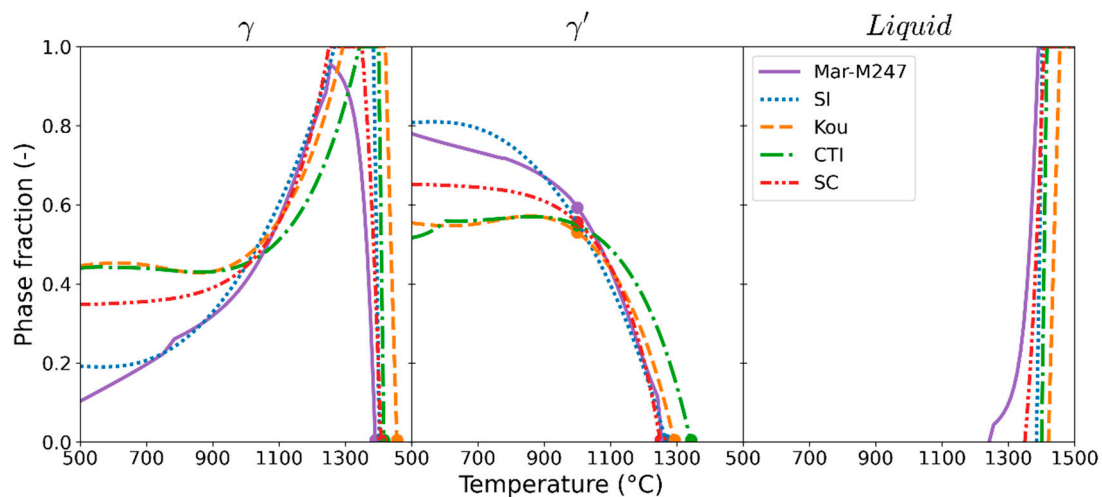


Figure 2. Phase fraction curves calculated with Thermo-Calc for liquid, γ , and γ' phases depending on temperature for reference alloy Mar-M247 and selected alloys. Properties used to define deviation from Mar-M247 are marked with dots.

Due to the differences in alloy compositions, developing a consistent etching procedure proved difficult. Therefore, the γ' phase fractions were not determined quantitatively. Nevertheless, qualitative image analysis showed that all alloys had high γ' content in the as-produced state. The microstructures of Mar-M247 and the SC alloy are presented in Figure 3. These are representative of the microstructures of all selected alloys.

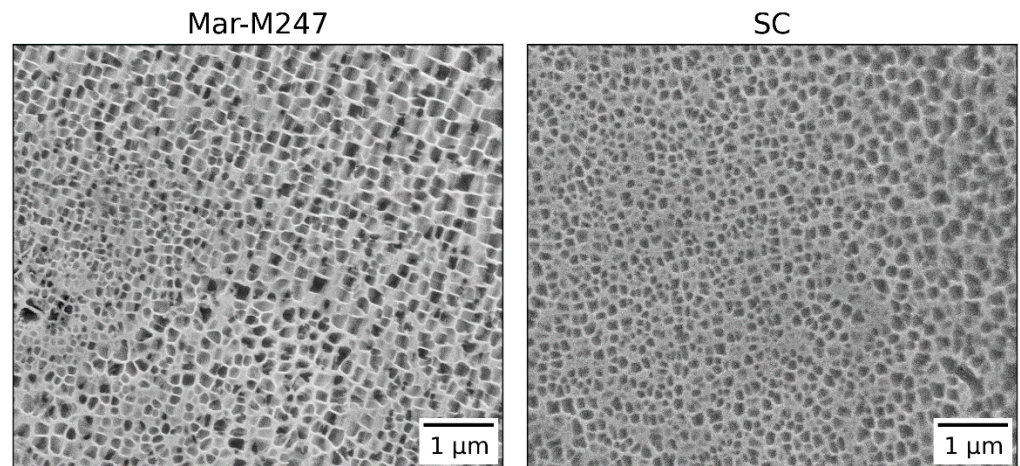


Figure 3. Microstructures of reference alloy Mar-M247 and SC alloy in as-cast state. γ matrix is light-colored, while γ' precipitates are dark. γ' phase fractions are high, as is typical for nickel-base superalloys.

3.2. DSC Analysis

DSC measurements of all alloys in the as-cast state were carried out to determine their solidification ranges (Figure 4). Since segregation in the as-cast alloys reflects the segregation due to non-equilibrium solidification, the alloys were not heat-treated. This makes it possible to assess the accuracy of the Scheil calculations.

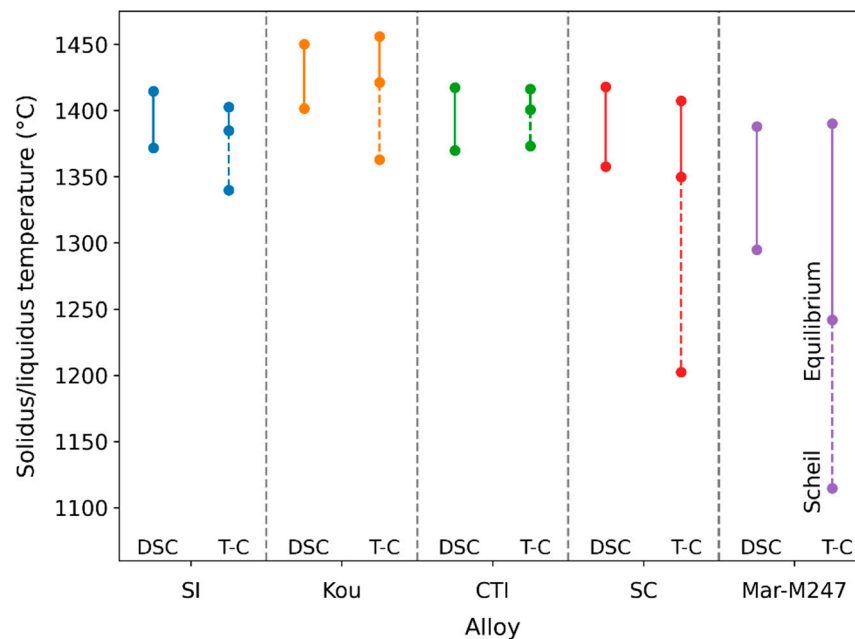


Figure 4. Solidus and liquidus temperatures measured with DSC and calculated with Thermo-Calc (T-C). Solidus temperatures were calculated in equilibrium and with Scheil solidification, where the temperature was determined at 95% solid phase fraction.

The liquidus temperature of all alloys was modeled quite accurately in the TCNI9 thermodynamic database. The accuracy of predicted solidus temperatures was mixed. For *SI* and *Kou* alloys, the measured solidus temperature was between the calculated values for equilibrium and Scheil solidification. For the *CTI* alloy, the Scheil calculation was more accurate than the equilibrium calculation. The picture changes for the *SC* alloy and Mar-M247. Here, the Scheil calculations predicted a far lower liquidus temperature

than that measured by DSC. However, due to the low heating rate, the DSC signal at low liquid fractions was very weak and may not have allowed exact determination of the solidus temperature.

The overall trends in transition temperatures are modeled well. It should be noted that Mar-M247 had both the lowest liquidus temperature and the widest solidification range. In general, the liquidus temperatures decreased and the solidification ranges increased with a higher content of alloying elements (cf. Table 3).

3.3. Cracking Susceptibility

The alloys were remelted in the as-produced state to determine their crack susceptibility. The measured crack densities are shown in Figure 5. The set energy input was much higher for the laser melting experiments than for electron beam melting to compensate for partial reflection and non-ideal absorptivity of the material. Therefore, the effective heat input was lower than indicated in Figure 5. The melt pool depths were lower in the laser-melted samples, since the specimens were at room temperature before melting, while in electron beam melting, the specimens were heated to at least 900 °C. Consequently, less heat was required to raise the temperature to the melting point in the latter case.

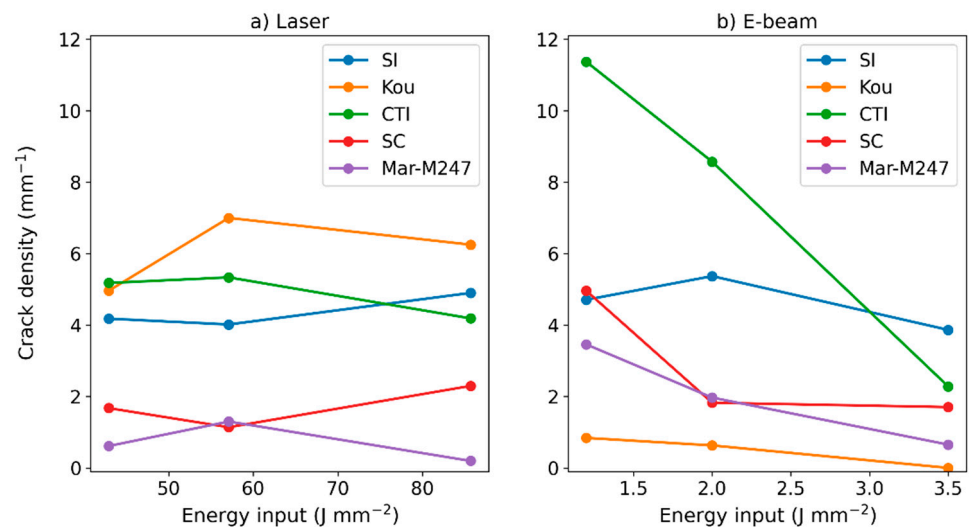


Figure 5. Crack density of experimental alloys and Mar-M247 from (a) laser and (b) electron beam melting experiments.

In the laser-remelted specimens, Mar-M247 alloy showed the lowest overall crack density at 0.2–1.3 mm⁻¹, followed by SC. The crack densities of the other experimental alloys were much higher at 4–7 mm⁻¹. There was no apparent correlation between energy input and crack density. Kou alloy exhibited the highest crack density. On the contrary, in the electron-beam-remelted specimens, Kou alloy had the lowest crack density (0–0.8 mm⁻¹). The trend in crack density for the remaining alloys was the same as for the laser-remelted specimens. The crack densities in both the laser- and electron-beam-remelted samples were quite similar, with CTI alloy melted at low energy input being the only exception. The crack densities decreased continuously with increasing energy input, except for the SI alloy.

Micrographs of cracks in the alloys after laser and electron beam remelting are presented in Figure 6. For the most part, cracks in the vicinity of the interface between the melt pool and non-melted base metal are shown, although the cracks often extend several 100 µm into the base metal. The cracks in the laser-melted alloys (SI, Kou, and CTI) have mostly straight crack flanks. This suggests that in these alloys, cracking in the solid state occurred rather than hot cracking. The cracks in Mar-M247 typically have a more jagged morphology that follows the dendrite structure. This is a characteristic sign of hot cracking. In contrast to the other alloys, Mar-M247 also showed multiple microscopic gaps between

cells or dendrites in the remelted area, which were probably caused by insufficient melt flow at the last stage of solidification.

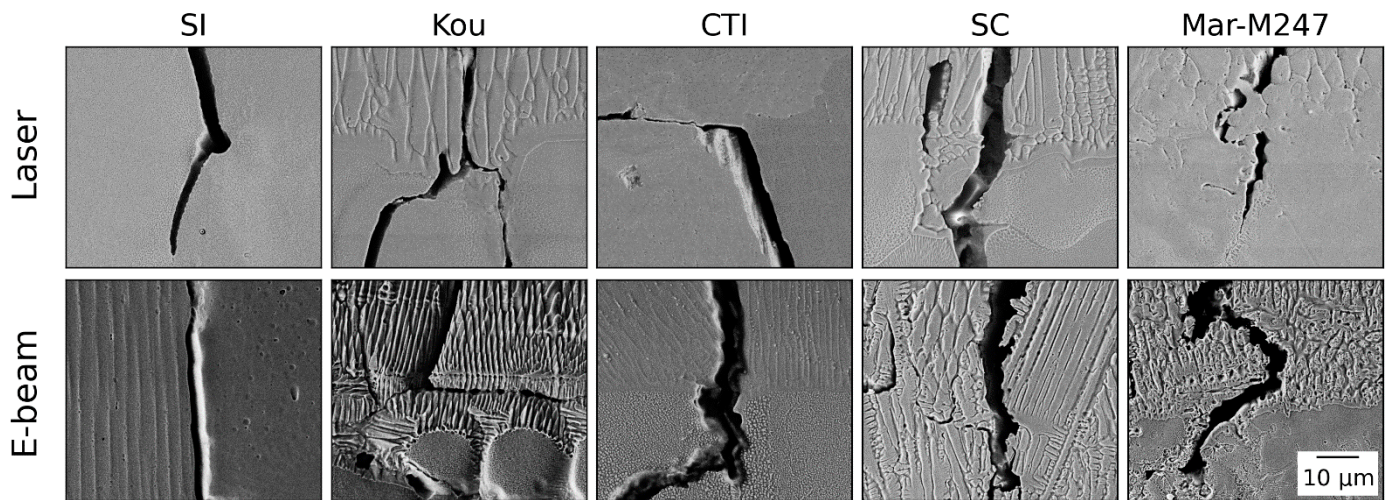


Figure 6. SEM micrographs of cracks in experimental alloys and reference Mar-M247 alloy from laser melting (**top** row) and electron beam melting (**bottom** row) experiments. All micrographs share the same scale bar.

The crack morphologies in the electron-beam-remelted samples appear slightly more tortuous than in the laser-remelted samples. This applies in particular to the *CTI*, *SC*, and *Mar-M247* alloys. The cracking mechanism cannot be determined unambiguously for *SI* and *Kou* since the solidification substructure is more cellular than dendritic, as it is in *SC* and *Mar-M247*. Therefore, solidification cracks will also develop straight crack flanks, conforming to the cellular solidification structure.

The crack tips in the laser-remelted specimens are often located within the base material at a distance of 100 µm or more from the melting interface. They are often found near islands of γ/γ' eutectic (Figure 7). On the contrary, the crack tips in the electron-beam-remelted specimens are usually located closer to the interface. The eutectic areas appear to be less extensive in *Kou* than in *Mar-M247*. In the electron-beam-remelted *Kou* specimen, no eutectic was apparent near the crack tips. The crack tips do not necessarily mark the origin of the cracks, since thermal shrinkage can pull the crack edges apart and thus drive the crack tip deeper into the material. Therefore, it can be assumed that the crack origin is located above the observed crack tip. As the laser melting was performed at room temperature, significant thermal shrinkage occurred, and long cracks were opened. During electron beam melting, less shrinkage occurred due to the high processing temperature of the material. The crack tips are most likely close to or at the true crack origin, which was located in the vicinity of the melting interface, within either the base metal or the remelted material.

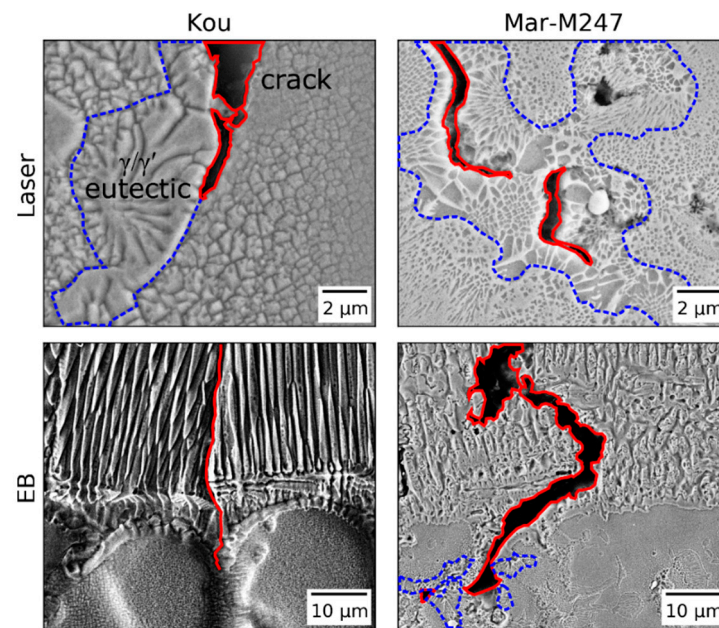


Figure 7. Details of crack tips and surrounding microstructure in *Kou* and *Mar-M247* alloys. Areas consisting of γ/γ' eutectic are marked in blue; cracks are highlighted in red.

4. Discussion

4.1. Cracking Mechanisms

The evaluation of crack morphology showed that the laser-remelted specimens developed primarily cold cracks, while in the electron-beam-remelted specimens, hot cracking was more prevalent. Furthermore, the alloys optimized for low cracking susceptibility often showed more cracks than the reference alloy *Mar-M247*, which is well known to be highly susceptible to cracking during AM [37]. However, excluding the minor elements B, C, and Zr could have reduced the cracking susceptibility of the alloy.

In the case of laser remelting, solidification cracking was the dominant mechanism only in *Mar-M247*. The initial assumption that hot cracking would be the leading cause of cracking was not met. Therefore, the optimization procedure was not able to identify alloys that are less vulnerable to cracking under these conditions since cold cracking was not included in the modeling. The hot cracking susceptibility of the experimental alloys during laser remelting could not be assessed. Comparing the crack densities (Figure 5) with the corresponding liquidus and solidus temperatures (Figure 4) suggests a close correlation between these quantities. This supports the observation of cold cracking: as soon as the temperature falls below the liquidus temperature and solid material forms, tensile strain builds up in the material due to thermal and solidification shrinkage. The total strain in the material at room temperature is closely related to the difference between liquidus and ambient temperature, as is the amount of solid-state cracks that form to alleviate the strain. There is no distinguishable influence of the heat input.

Overall, electron beam remelting caused similar crack densities as laser remelting. However, the processing conditions are not directly comparable, since the energy input per unit area and the temperature of the build chamber were very different. Nonetheless, most alloys exhibit a trend of monotonically decreasing crack density with increasing heat input. This phenomenon can be related to the stress state in the material. A lower heat input leads to higher thermal gradients and higher thermal strain, which tear the material apart at weak points such as liquid films between dendrites.

For both laser and electron beam melting, the crack tips are often located next to areas of γ/γ' eutectic (Figure 7). Li et al. [6] suggested a crack initiation mechanism related to these eutectic islands. The eutectic has a low melting point. During the melting of one layer, the eutectic in the heat-affected zone (HAZ) can be molten locally and form intergranular

liquid films, which lack the strength to resist grain boundary decohesion. Tensile strain caused by thermal shrinkage in the horizontal direction pulls the grains apart. Since these cracks originate in the HAZ, they can be classified as liquation cracks. Liquation cracking may have occurred in some instances during electron beam remelting. Considering the laser melting experiments, the influence of this effect is inconclusive, as the exact crack origin can hardly be determined.

Liquation cracking was not explicitly considered in the cracking models. However, the presence of eutectic usually extends the Scheil solidification range. Conversely, a reduction in the solidification range, as was achieved for the *SI*, *CTI*, and *Kou* alloys, should also reduce the amount of eutectic present. Hence, the three criteria, *SI*, *CTI*, and *Kou*, also indirectly minimize the liquation cracking susceptibility.

4.2. Correlation Analysis

A quantitative analysis of the correlations between measured crack densities and various cracking criteria is shown in Figure 8. The top panel presents the mean measured crack densities. The heat map below shows the values of the different cracking criteria as calculated with Thermo-Calc. Since their absolute values span several orders of magnitude, they were normalized from 0 to 1 to allow for better comparability. The cracking criteria are abbreviated as follows: $T_L - T_S$ is the solidification interval, $\max |dT/df_s|$ is the Kou criterion, ΔT_c is the critical temperature interval, and $\Delta\epsilon/\Delta T$ is the shrinkage coefficient. The criterion values of the experimental alloys are outlined in gray. In addition to the four criteria defined in Section 2.1, the liquidus temperature (T_L) and γ' solvus temperature ($T_{\gamma'}$) were calculated for each alloy. The rank correlation ρ between crack densities and cracking criteria, according to Spearman, is shown on the right. The rank correlation between two quantities indicates whether an increase in one quantity also leads to an increase in the other. In the context of optimization, we are primarily interested in a rank correlation instead of, e.g., a stronger linear correlation between the predictor values and the predicted properties. A rank correlation is sufficient for an optimization algorithm to find the alloys with the best properties based on the respective predictor values.

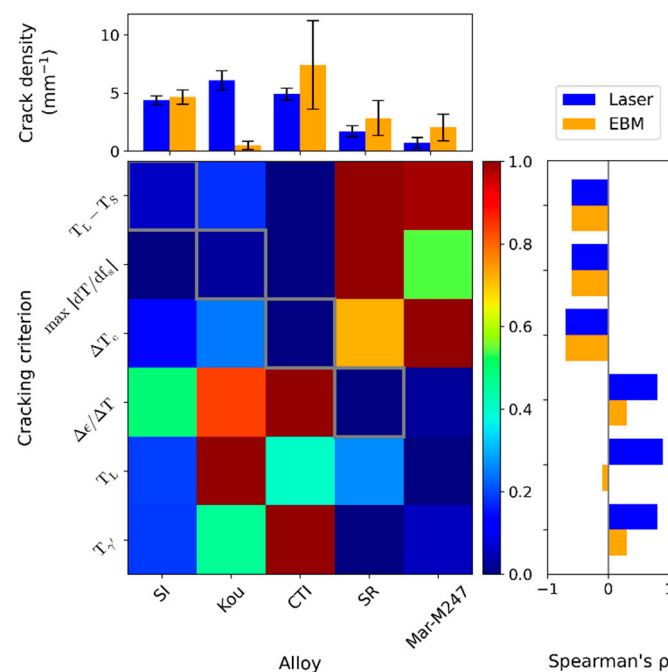


Figure 8. Correlation analysis of experimentally determined crack densities with calculated, normalized cracking criteria. $T_L - T_S$, solidification interval; $\max |dT/df_s|$, Kou criterion; $\Delta T/\Delta f_s$, critical temperature interval; and $\Delta\epsilon/\Delta T$, shrinkage coefficient.

The solidification interval, Kou criterion, and critical temperature interval criterion all negatively correlate with the crack densities. Here, a good low value for a cracking criterion predicts high crack density. In contrast, the remaining criteria correlate positively with the crack densities of the laser-remelted specimens. The positive correlations are only marginal for the electron-beam-melted specimens. The correlation coefficient of the liquidus temperature is slightly negative due to the low crack density in the *Kou* alloy.

It is not trivial to discriminate between causation and pure correlation of the cracking criteria. The liquidus temperature, displaying the greatest correlation in laser remelting, is probably the main cause of cracking, as explained above. In contrast, lower values of the first three cracking criteria are not causally responsible for higher crack densities. These criteria (*SI*, *Kou*, *CTI*) will generally improve with reduced additions of alloying elements. Simultaneously, this will lead to a higher liquidus temperature. Therefore, the apparent negative correlation with the crack density is due to an indirect correlation of the respective criteria with the liquidus temperature rather than being an actual cause of cracking. A similar behavior was seen in the design of a FeCrAl alloy for AM [38]. Here, an alloy optimized for the minimal solidification range and a shallow gradient dT/df_s to achieve improved printability by SLM did not develop any hot cracks but was sensitive to cold cracking. This alloy also exhibited a significantly higher liquidus temperature than commercially available steels, affirming that an increase in liquidus temperature promotes cold cracking.

The shrinkage coefficient criterion exhibits a positive correlation with the crack density. A causal relation is plausible, since a lower thermal shrinkage coefficient $d\varepsilon/dT$ reduces the strain rate during cooling and allows for sufficient liquid feeding in the interdendritic space, which in turn will reduce cracking [28].

Upon precipitation of the γ' phase, the thermal expansion coefficient increases sharply, causing a stronger contraction of the material [39] and, therefore, greater strain. The higher the γ' solvus temperature, the earlier this jump occurs during cooling and the greater the accumulated strain. This could explain a positive correlation with the crack density. However, at cooling rates typically encountered during AM and in this study, the γ' precipitation is partially suppressed [40]. Therefore, it is unclear whether there is a causal relation between γ' solvus temperature and crack density.

The correlations of shrinkage coefficient, liquidus temperature, and γ' solvus temperature with the crack densities of electron-beam-remelted specimens are not deemed significant. Nonetheless, the extremely small number of cracks found in the *Kou* alloy, which, conversely, exhibited the highest crack density after laser remelting, suggests that existing cracking models can assist in designing crack-resistant alloys with a high γ' fraction. It is essential that these models reflect the actual cracking mechanisms, which highly depend on the processing conditions. Alloys ready for application will require the consideration of additional properties such as creep strength and oxidation resistance.

5. Conclusions

Four criteria for solidification cracking from the literature based on Scheil solidification were implemented in multi-criteria optimization software for alloy development. For each criterion, multi-criteria optimization was carried out to minimize the cracking susceptibility while keeping several crucial properties close to those of the reference material, Mar-M247. The alloys were cast and remelted by laser at room temperature and electron beam at 900 °C to study their cracking behavior under conditions close to additive manufacturing. Finally, the correlations between the cracking indicators and the measured crack densities were analyzed. The following conclusions can be drawn:

- Hot cracking occurred predominantly during electron beam melting at high process temperature, while only cold cracking was observed after laser melting due to the low process temperature. No improvement in cracking susceptibility could be achieved for laser melting.
- The hot cracking susceptibility of the alloy based on the Kou criterion could be improved compared to the reference Mar-M247 alloy under electron beam melting conditions.

- Most cracking criteria favor low-alloy compositions, which lead to high solidus and liquidus temperatures. Therefore, the susceptibility to cold cracking is increased.
- In order to develop alloys suitable for real applications, the cracking indicator must be chosen based on the expected cracking mechanism or should reflect multiple possible mechanisms. Furthermore, mechanical or corrosion properties must be considered.

Author Contributions: Conceptualization, B.W. and M.M.; methodology, B.W. and D.L.; software, B.W.; formal analysis, B.W. and D.L.; investigation, B.W. and D.L.; writing—original draft preparation, B.W.; writing—review and editing, M.M. and C.K.; visualization, B.W.; supervision, M.M. and C.K.; project administration, M.M.; funding acquisition, M.M. and C.K. All authors have read and agreed to the published version of the manuscript.

Funding: This research was funded by the German Research Foundation (DFG).

Institutional Review Board Statement: Not applicable.

Informed Consent Statement: Not applicable.

Data Availability Statement: The data presented in this study are available on request from the corresponding author.

Acknowledgments: We gratefully acknowledge the German Research Foundation (DFG) and the Collaborative Research Center 103 Project C7. The DFG instrument grant INST 90/987-1 FUGG (purchase of the LMD instrument) is also acknowledged. We further thank Florian Galgon for his support in conducting the laser melting trials and Jakob Renner and Daniel Gage for the electron beam melting trials.

Conflicts of Interest: The authors declare no conflict of interest. The funders had no role in the design of the study; in the collection, analyses, or interpretation of data; in the writing of the manuscript, or in the decision to publish the results.

References

1. Chauvet, E.; Tassin, C.; Blandin, J.-J.; Dendievel, R.; Martin, G. Producing Ni-base superalloys single crystal by selective electron beam melting. *Scr. Mater.* **2018**, *152*, 15–19. [[CrossRef](#)]
2. Körner, C.; Ramsperger, M.; Meid, C.; Bürger, D.; Wollgramm, P.; Bartsch, M.; Eggeler, G. Microstructure and mechanical properties of CMSX-4 single crystals prepared by additive manufacturing. *Metall. Mater. Trans. A* **2018**, *49*, 3781–3792. [[CrossRef](#)]
3. Gotterbarm, M.R.; Rausch, A.M.; Körner, C. Fabrication of Single Crystals through a μ -Helix Grain Selection Process during Electron Beam Metal Additive Manufacturing. *Metals* **2020**, *10*, 313. [[CrossRef](#)]
4. Kontis, P.; Chauvet, E.; Peng, Z.; He, J.; da Silva, A.K.; Raabe, D.; Tassin, C.; Blandin, J.-J.; Abed, S.; Dendievel, R.; et al. Atomic-scale grain boundary engineering to overcome hot-cracking in additively manufactured superalloys. *Acta Mater.* **2019**, *177*, 209–221. [[CrossRef](#)]
5. Chen, Y.; Lu, F.; Zhang, K.; Nie, P.; Hosseini, S.R.E.; Feng, K.; Li, Z. Dendritic microstructure and hot cracking of laser additive manufactured Inconel 718 under improved base cooling. *J. Alloys Compd.* **2016**, *670*, 312–321. [[CrossRef](#)]
6. Li, Y.; Chen, K.; Tamura, N. Mechanism of heat affected zone cracking in Ni-based superalloy DZ125L fabricated by laser 3D printing technique. *Mater. Des.* **2018**, *150*, 171–181. [[CrossRef](#)]
7. Chen, Y.; Zhang, K.; Huang, J.; Hosseini, S.R.E.; Li, Z. Characterization of heat affected zone liquation cracking in laser additive manufacturing of Inconel 718. *Mater. Des.* **2016**, *90*, 586–594. [[CrossRef](#)]
8. Zhang, X.; Chen, H.; Xu, L.; Xu, J.; Ren, X.; Chen, X. Cracking mechanism and susceptibility of laser melting deposited Inconel 738 superalloy. *Mater. Des.* **2018**, *183*, 108105. [[CrossRef](#)]
9. Chauvet, E.; Kontis, P.; Jäggle, E.A.; Gault, B.; Raabe, D.; Tassin, C.; Blandin, J.-J.; Dendievel, R.; Vayre, B.; Abed, S.; et al. Hot cracking mechanism affecting a non-weldable Ni-based superalloy produced by selective electron beam melting. *Acta Mater.* **2018**, *142*, 82–94. [[CrossRef](#)]
10. Ojo, O.A.; Richards, N.L.; Chaturvedi, M.C. Study of the fusion zone and heat-affected zone microstructures in tungsten inert gas-welded INCONEL 738LC superalloy. *Metall. Mater. Trans. A* **2006**, *37*, 421–433. [[CrossRef](#)]
11. Li, C.; Liu, Z.Y.; Fang, X.Y.; Guo, Y.B. Residual stress in metal additive manufacturing. *Procedia CIRP* **2018**, *71*, 348–353. [[CrossRef](#)]
12. Yokokawa, T.; Harada, H.; Kawagishi, K.; Kobayashi, T.; Yuyama, M.; Takata, Y. Advanced Alloy Design Program and Improvement of Sixth-Generation Ni-Base Single Crystal Superalloy TMS-238. In *Superalloys 2020*; Tin, S., Hardy, M., Clews, J., Cormier, J., Feng, Q., Marcin, J., O'Brien, C., Suzuki, A., Eds.; Springer: Cham, Switzerland, 2020; pp. 122–130.
13. Reed, R.C.; Tao, T.; Warnken, N. Alloys-by-design: Application to nickel-based single crystal superalloys. *Acta Mater.* **2009**, *57*, 5898–5913. [[CrossRef](#)]

14. Tang, Y.T.; Panwisawas, C.; Ghossoub, J.N.; Gong, Y.; Clark, J.W.; Németh, A.A.N.; McCartney, D.G.; Reed, R.C. Alloys-by-design: Application to new superalloys for additive manufacturing. *Acta Mater.* **2021**, *202*, 417–436. [[CrossRef](#)]
15. Alabort, E.; Barba, D.; Shagiev, M.R.; Murzinova, M.A.; Galejev, R.M.; Valiakhmetov, O.R.; Aletdinov, A.F.; Reed, R.C. Alloys-by-design: Application to titanium alloys for optimal superplasticity. *Acta Mater.* **2019**, *178*, 275–287. [[CrossRef](#)]
16. Rettig, R.; Ritter, N.C.; Helmer, H.E.; Neumeier, S.; Singer, R.F. Single-crystal nickel-based superalloys developed by numerical multi-criteria optimization techniques: Design based on thermodynamic calculations and experimental validation. *Modell. Simul. Mater. Sci. Eng.* **2015**, *23*, 035004. [[CrossRef](#)]
17. Menou, E.; Toda-Caraballo, I.; Rivera-Díaz-del, P.E.J.; Pineau, C.; Bertrand, E.; Ramstein, G.; Tancret, F. Evolutionary design of strong and stable high entropy alloys using multi-objective optimisation based on physical models, statistics and thermodynamics. *Mater. Des.* **2018**, *143*, 185–195. [[CrossRef](#)]
18. Markl, M.; Müller, A.; Ritter, N.; Hofmeister, M.; Naujoks, D.; Schaar, H.; Abrahams, K.; Frenzel, J.; Subramanyam, A.P.A.; Ludwig, A.; et al. Development of single-crystal Ni-base superalloys based on multi-criteria numerical optimization and efficient use of refractory elements. *Metall. Mater. Trans. A* **2018**, *49*, 4134–4145. [[CrossRef](#)]
19. Müller, A.; Roslyakova, I.; Sprenger, M.; Git, P.; Rettig, R.; Markl, M.; Körner, C.; Singer, R.F. MultOpt++: A fast regression-based model for the development of compositions with high robustness against scatter of element concentrations. *Modell. Simul. Mater. Sci. Eng.* **2019**, *27*, 024001. [[CrossRef](#)]
20. Rettig, R.; Matuszewski, K.; Müller, A.; Helmer, H.E.; Ritter, N.C.; Singer, R.F. Development of a low-density rhenium-free single crystal nickel-based superalloy by application of numerical multi-criteria optimization using thermodynamic calculations. In *Superalloys 2016*; Hardy, M., Huron, E., Glatzel, U., Griffin, B., Lewis, B., Rae, C., Seetharaman, V., Tin, S., Eds.; John Wiley & Sons: Hoboken, NJ, USA, 2016; pp. 35–44.
21. Basak, C.B.; Krishnan, M. Applicability of Scheil–Gulliver solidification model in real alloy: A case study with Cu-9wt% Ni-6wt% Sn alloy. *Philos. Mag. Lett.* **2015**, *95*, 376–383. [[CrossRef](#)]
22. Ghossoub, J.N.; Tang, Y.T.; Panwisawas, P.; Németh, A.; Reed, R.C. On the influence of alloy chemistry and processing conditions on additive manufacturability of Ni-based superalloys. In *Superalloys 2020*; Tin, S., Hardy, M., Clews, J., Cormier, J., Feng, Q., Marcin, J., O'Brien, C., Suzuki, A., Eds.; Springer: Cham, Switzerland, 2020; pp. 153–162.
23. Kou, S. A simple index for predicting the susceptibility to solidification cracking. *Weld. J.* **2015**, *94*, 374–388.
24. Kou, S. A criterion for cracking during solidification. *Acta Mater.* **2015**, *88*, 366–374. [[CrossRef](#)]
25. Xia, C.; Kou, S. Evaluating susceptibility of Ni-base alloys to solidification cracking by transverse-motion weldability test. *Sci. Tech. Weld. Join.* **2020**, *25*, 690–697. [[CrossRef](#)]
26. Shukla, A.; Sarkar, S.; Durga, A.; Adharapurapu, R.; Dial, L.; Sondhi, S.K. Computational design of additively printable nickel superalloys. In *Superalloys 2020*; Tin, S., Hardy, M., Clews, J., Cormier, J., Feng, Q., Marcin, J., O'Brien, C., Suzuki, A., Eds.; Springer: Cham, Switzerland, 2020; pp. 1066–1074.
27. Zhang, J.; Singer, R.F. Hot tearing of nickel-based superalloys during directional solidification. *Acta Mater.* **2002**, *50*, 1869–1879. [[CrossRef](#)]
28. Rappaz, M.; Drezet, J.M.; Gremaud, M. A new hot-tearing criterion. *Metall. Mater. Trans. A* **1999**, *30*, 449–455. [[CrossRef](#)]
29. Harris, K.; Erickson, G.L.; Schwer, R.E. MAR-M247 derivations—CM247 LC DS alloy, CMSX single crystal alloys, properties and performance. In *Superalloys 1984*; Gell, M., Ed.; Metallurgical Society of AIME: Englewood, NJ, USA, 1984; pp. 221–230.
30. Andersson, J.O.; Helander, T.; Höglund, L.; Shi, P.; Sundman, B. Thermo-Calc & DICTRA, computational tools for materials science. *Calphad* **2002**, *26*, 273–312.
31. Blank, J.; Deb, K. pymoo: Multi-objective optimization in python. *IEEE Access* **2020**, *8*, 89497–89509. [[CrossRef](#)]
32. Deb, K.; Pratap, A.; Agarwal, S.; Meyarivan, T.A.M.T. A fast and elitist multiobjective genetic algorithm: NSGA-II. *IEEE Trans. Evol. Comput.* **2002**, *6*, 182–197. [[CrossRef](#)]
33. Auger, A.; Bader, J.; Brockhoff, D.; Zitzler, E. Hypervolume-based multiobjective optimization: Theoretical foundations and practical implications. *Theor. Comput. Sci.* **2012**, *425*, 75–103. [[CrossRef](#)]
34. Helmer, H.E.; Körner, C.; Singer, R.F. Additive manufacturing of nickel-based superalloy Inconel 718 by selective electron beam melting: Processing window and microstructure. *J. Mater. Res.* **2014**, *29*, 1987–1996. [[CrossRef](#)]
35. Arnold, C.; Pobel, C.; Osmanlic, F.; Körner, C. Layerwise monitoring of electron beam melting via backscatter electron detection. *Rapid Prototyp. J.* **2018**, *24*, 1401–1406. [[CrossRef](#)]
36. Rachmawati, L.; Srinivasan, D. Multiobjective evolutionary algorithm with controllable focus on the knees of the Pareto front. *IEEE Trans. Evol. Comput.* **2009**, *13*, 810–824. [[CrossRef](#)]
37. Seidel, A.; Finaske, T.; Straubel, A.; Wendrock, H.; Maiwald, T.; Riede, M.; Lopez, E.; Brueckner, F.; Leyens, C. Additive manufacturing of powdery Ni-based superalloys Mar-M-247 and CM 247 LC in hybrid laser metal deposition. *Metall. Mater. Trans. A* **2018**, *49*, 3812–3830. [[CrossRef](#)]
38. Dovggy, B.; Simonelli, M.; Pham, M.S. Alloy design against the solidification cracking in fusion additive manufacturing: An application to a FeCrAl alloy. *Mater. Res. Lett.* **2021**, *9*, 350–357. [[CrossRef](#)]
39. Horst, O.M.; Schmitz, D.; Schreuer, J.; Git, P.; Wang, H.; Körner, C.; Eggeler, G. Thermoelastic properties and γ' -solvus temperatures of single-crystal Ni-base superalloys. *J. Mater. Sci.* **2021**, *56*, 7637–7658. [[CrossRef](#)]
40. Divya, V.D.; Muñoz-Moreno, R.; Messé, O.M.D.M.; Barnard, J.S.; Baker, S.; Illston, T.; Stone, H.J. Microstructure of selective laser melted CM247LC nickel-based superalloy and its evolution through heat treatment. *Mater. Charact.* **2016**, *114*, 62–74. [[CrossRef](#)]